Article

Not peer-reviewed version

A Tale of Two Hemispheres: Asymmetric Geospace Responses and the GNSS Paradox of the October 2024 Severe Geomagnetic Storm

Joseph Omojola * and Daniel Moeketsi

Posted Date: 30 March 2026

doi: 10.20944/preprints202603.2324.v1

Keywords: geomagnetic storm; ionosphere-thermosphere coupling; ionosphere hemispheric asymmetry; total electron content

 doi:10.20944/preprints202603.2324.v1

Article

A Tale of Two Hemispheres: Asymmetric Geospace Responses and the GNSS Paradox of the October 2024 Severe Geomagnetic Storm

Joseph Omojola [1,2]* and Daniel Moeketsi [1]

[1] Centre for Space Research, North-West University, Potchefstroom Campus, South Africa
[2] Department of Physics, Federal University of Lafia, Nasarawa State, Nigeria
* Correspondence: omojola.josef@gmail.com; Tel.: +27-679315161

Abstract

Space weather events triggered by solar activity impact critical technologies like the Global Navigation Satellite System (GNSS) by causing atmospheric imbalances that alter ionospheric electron density. This study investigates the geospace response to the severe geomagnetic storms of October 2024, focusing on the coupling and compositional exchange between the ionosphere and thermosphere. Data were analyzed from two near-magnetic conjugate mid-latitude African stations, Rabat (RABT) and Hermanus (HNUS), using GNSS-TEC measurements alongside thermospheric circulation observations from NASA GOLD and solar wind indices from OMNIWeb. The October 2024 storm, which reached a minimum Dst of -333 nT, drove a negative ionospheric storm phase marked by Total Electron Content (TEC) depletions exceeding 50 TECU. This response was driven by storm-time thermospheric upwelling of N_2-rich air, which lowered the O/N_2 ratio and accelerated plasma loss via charge-exchange reactions. Furthermore, a distinct hemispheric asymmetry was observed, as the equatorward thermospheric circulation in the Northern Hemisphere arrived before that of the Southern Hemisphere. Direct post-processing of ECEF coordinates using RTKLIB revealed a "GNSS Paradox": while positioning accuracy significantly degraded at HNUS with errors increasing by up to 270%, it counterintuitively improved at RABT, where errors reached their minimum during the main and early recovery phases of the storm. These findings highlight that the technological impact of severe space weather is determined not just by storm magnitude, but by the specific sign and spatial structure of the regional ionospheric response.

Keywords: geomagnetic storm; ionosphere-thermosphere coupling; ionosphere hemispheric asymmetry; total electron content

1. Introduction

Space weather events are recognised phenomena that impact space technology, including the Global Navigation Satellite System (GNSS) and high-frequency radio communications, affecting human activities reliant on these technologies. These events are triggered by solar activity, such as solar flares (SFs) and coronal mass ejections (CMEs) e.g. [15].

Solar flares are large bursts of electromagnetic energy, often followed by coronal mass ejections (CMEs). During these CMEs, the increased levels of solar wind particles exert additional pressure on the magnetosphere, resulting in the significant compression of the magnetopause [35]. A southward-oriented interplanetary magnetic field (Bz) leads to magnetic reconnection on the day side of the Earth. This process causes geomagnetic storms and results in particle precipitation from the turbulent solar wind. The increased charged particle density initiates atmospheric dynamics that create an imbalance in the thermosphere, affecting the distribution of atmospheric molecules, ions, and atoms on short- and long-term scales e.g. [9,12,28,30]. Since the thermosphere and the ionosphere are energetically

 doi:10.20944/preprints202603.2324.v1

coupled through solar irradiance and geomagnetic activity, the ionosphere can be severely affected during such geomagnetic disturbance e.g. [22,35].

A geomagnetic storm can drive the inflow of energetic particles into the high-latitude upper atmosphere, initiating a nucleonic electromagnetic cascade that changes atmospheric chemistry e.g. [11,24,36] and dynamics by the equatorward thermospheric circulation e.g.[26]. High-energy charged particles,initiate this cascade in the ionosphere. As a result, the ionosphere's total electron content (TEC) is altered, resulting in temporal and spatial fluctuations in electron density e.g. [20]. The sudden changes in the F-region and the ionosphere's response can increase group delay in Global Navigation Satellite Systems (GNSS) or a complete blackout of high-frequency radio communication e.g. [17,21], depending on whether the TEC is enhanced or depleted, respectively. Fluctuations in TEC have become a significant topic in space weather physics, with various models explaining the depletion or enhancement of TEC through thermospheric circulation and variations in the O/N_2 ratio e.g. [8,10,19,29].

The ionosphere-thermosphere (IT) system responds dramatically to geomagnetic disturbances. Energy deposition at high latitudes through Joule heating and particle precipitation drives to thermospheric expansion and circulation divergence, leading to upwelling. This upwelling transports air rich in molecular nitrogen (N_2) from lower altitudes to the F-region, lowering the crucial O/N_2 ratio [4,6,26]. Accurate representation of the ionospheric state during the main phase of geomagnetic storms remains a significant challenge, as the system is strongly influenced by localised processes such as neutral winds and electric field that are difficult to capture. While studies have demonstrated that assimilating thermospheric mass density (TMD) from satellites into physics-based models like the Coupled Thermosphere Ionosphere Plasmasphere electrodynamics (CTIPe) can enhance global upper atmospheric representations [5], these models are often not fully constrained by TMD alone. Consequently, global models may overlook regional dynamics, such as the specific inter-hemispheric timing of wind surges e.g. [5,33]. This highlights the critical need for direct, high-resolution observations of thermospheric circulation and compositional exchange provided in this study through NASA GOLD and ground-based GNSS-TEC measurements to resolve the complex, localised IT coupling over mid-latitude sectors.

A decreased O/N_2 ratio is the signature of a negative ionospheric storm because molecular ions (NO^+ and O_2^+) resulting from charge exchange reactions ($O^+ + N_2 \rightarrow NO^+ + N$) recombine with electrons much faster than atomic oxygen ions (O^+) do e.g. [7,34], depleting the total electron content (TEC). Conversely, equatorward neutral winds driven by storm-time heating can push plasma upward along magnetic field lines, reducing the ion recombination rate and causing positive storms (TEC enhancement) e.g. [8,26].

The thermospheric and ionospheric responses over the European sector during the G3-level extreme geomagnetic storm of November 3–4, 2021 was reported in [14], in which they identified two antithetical ionospheric storm phases. At high latitudes, negative ionospheric storms occurred due to thermospheric heating and upwelling, which reduced the O/N_2 ratio and accelerated plasma loss. In contrast, middle and low latitudes experienced positive ionospheric storms driven by equatorward and westward neutral winds that transported plasma to higher altitudes along magnetic field lines where recombination rates are lower, effectively prolonging the plasma lifetime. The findings suggest that negative and positive ionospheric storms are not isolated events but are interconnected through simultaneous regional changes in thermospheric composition and wind dynamics e.g. [14,16].

Storm-time TEC fluctuation is linked to the changes in the molecular nitrogen (N_2), where an increase in N_2 due to faster ion recombination led to a depletion in the upper atmosphere TEC e.g. [6,18,26] During a severe geomagnetic storm, particle precipitation from solar wind charged particles occurs, particularly in the high-latitude ionosphere e.g. [11,36], and sometimes reaches low latitudes e.g. [31]. This particle precipitation often led to sudden fluctuation of atmospheric constituents at lower altitude [11].

 doi:10.20944/preprints202603.2324.v1

In this study, we analyze the October 2024 storm using conjugate mid-latitude stations to resolve the inter-hemispheric timing of thermospheric surges. This study is crucial for understanding sudden changes in the upper atmosphere, which drive either depletion or enhancement of TEC that affects GNSS signals and high-frequency radio communication e.g. [9,13].

2. Materials and Methods

2.1. Observations and Data Analysis

This study utilises GNSS data obtained from two stations in the mid-latitude African sector: one in Rabat, Morocco, with station ID RABT, and the other in Hermanus, South Africa, with station ID HNUS. Both stations are located in the Northern and Southern Hemispheres, respectively, and are near magnetic conjugates in latitude (see Figure 1).

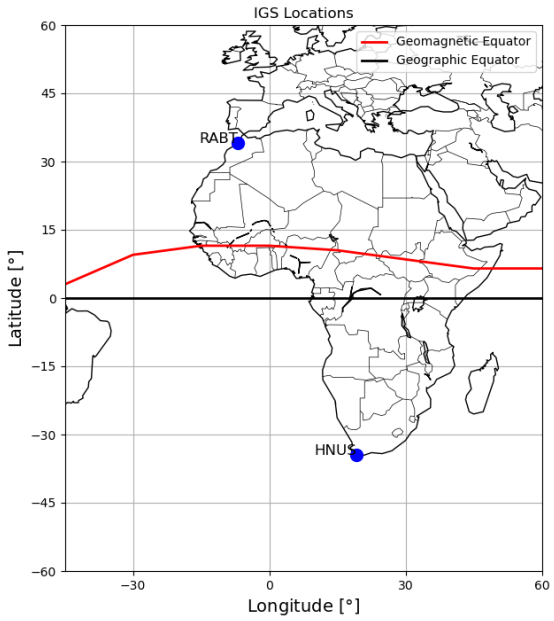

Figure 1. The Map of Africa showing the locations of the two IGS stations. The map illustrates the relationship of the stations to both the geomagnetic and geographic equators.

2.2. October 2024 Events

The October severe storm was associated with multiple CMEs and an eruption from AR 13848 on 9 October, distinguished by its strong X-ray brightness[1]. This event unfolded as a two-step storm: first, a moderate sudden storm commencement (SSC) with a minimum *Dst* of -148 nT on October 8 (DOY 282), followed by a more intense SSC that produced a minimum *Dst* of -333 nT on October 11 (DOY 285) (see Figure 2).

[1] https://solarmonitor.org/data/

 doi:10.20944/preprints202603.2324.v1

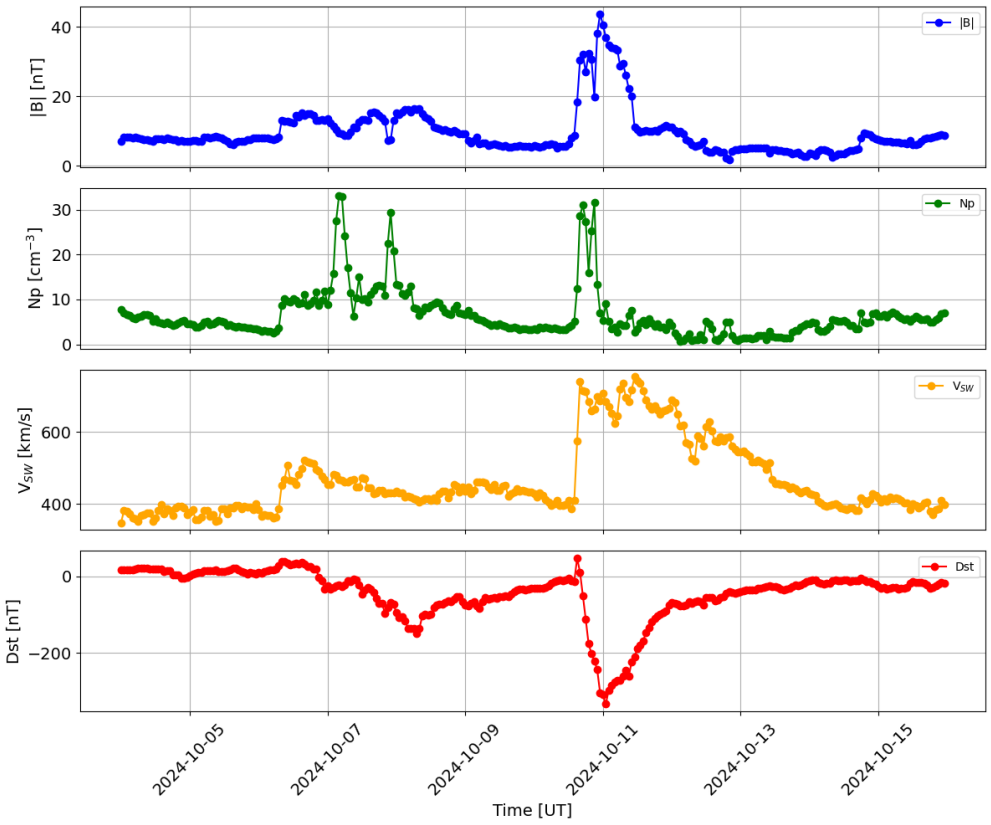

Figure 2. The space weather characteristics during the event in October 2024. $|B|$ is the interplanetary magnetic field, N_p is the proton density, while V_{sw} is the solar wind speed, and the disturbed storm time index, *Dst*, on October 5 - 15, 2024.

2.3. Data Sources and Analysis

The space weather parameters were obtained from the OMNIWeb data service[2]. The GNSS-TEC data were obtained from the International GNSS Stations (IGS[3]) and IONOLAB[4] [1,2,32] for the two stations This data was used to estimate the storm-time temporal fluctuations in TEC. While the TEC is the integrated electron density along the ray path between the GNSS satellite in space and the receiver on the ground, which is usually expressed in TEC units (TECU), where 1TECU = 1×10^{16} electrons/m^2.

Data from NASA Global-Scale Observations of the Limb and Disk (NASA-GOLD[5]) were analysed for the storm-time thermospheric circulation and fluctuations.

In a single-point positioning technique, we utilised RTKLIB[6] for post-processing with a 15° elevation mask angle, ensuring that at least five GNSS satellites were visible (data quality factor) to assess the positioning accuracy of the station following the methodologies outlined in [25,26]. Additionally, we determine the storm-time positioning error on the Earth Centred Earth Fixed (ECEF) coordinates using the differences between the coordinates obtained during the post-processing of the stations' observations and navigational files and the station position given by International Terrestrial Reference Frame (ITRF) coordinates[7].

[2] https://omniweb.gsfc.nasa.gov/form/dx1.html
[3] https://cddis.nasa.gov/archive/gnss/data/daily/
[4] http://ionolab.org/index.php?page=webtec&language=en
[5] https://gold.cs.ucf.edu/data/
[6] https://www.rtklib.com
[7] https://network.igs.org

 doi:10.20944/preprints202603.2324.v1

3. Results

3.1. October 2024 Geomagnetic Storm Events

The October 2024 severe geomagnetic storm developed as a distinct two-step event. The first step was triggered by a moderate Sudden Storm Commencement (SSC) at 08:00 UT on October 6 (DOY 280), characterised by an immediate rise in solar wind speed to approximately 452 km/s (see Figure 2). This initial disturbance led to the onset of the main phase at 04:00 UT on October 7 as proton density peaked at 33 cm^{-3}[3], eventually reaching a minimum *Dst* of -148 nT by the morning of October 8. After a short recovery period, a second and significantly more severe phase commenced at 16:00 UT on October 10 (DOY 284), with the interplanetary magnetic field ($|B|$) intensifying to 32 nT and solar wind speeds (V_{sw}) surging to 740 km/s. This second step drove the storm to its absolute peak, reaching a severe minimum *Dst* of -333 nT at 01:00 UT on October 11 (DOY 285).

The thermospheric circulation patterns shown in Figures 3–5 for the main phase of the October 11 (DOY 285) storm indicate that N_2-dominated winds are transported equatorward in both hemispheres. Unlike the extreme May storm where the equatorward thermospheric wind advected from the Southern Hemisphere arrive earlier than that of the Northern Hemisphere [26], however, the equatorward thermospheric flow during the October event from the Northern Hemisphere reached earlier than the Southern Hemisphere (see Figure 4).

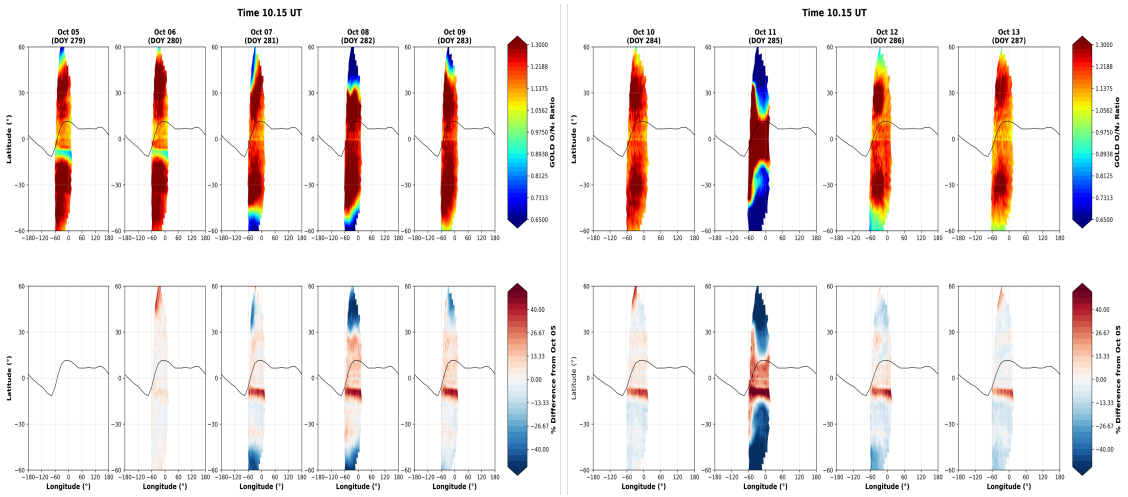

Figure 3. Thermospheric circulations during the October 2024 geomagnetic storm at 10.15 UT. The plot from NASA-GOLD illustrates the thermospheric circulation patterns observed from October 5 to October 13 (DOY 279 - 287).

 doi:10.20944/preprints202603.2324.v1

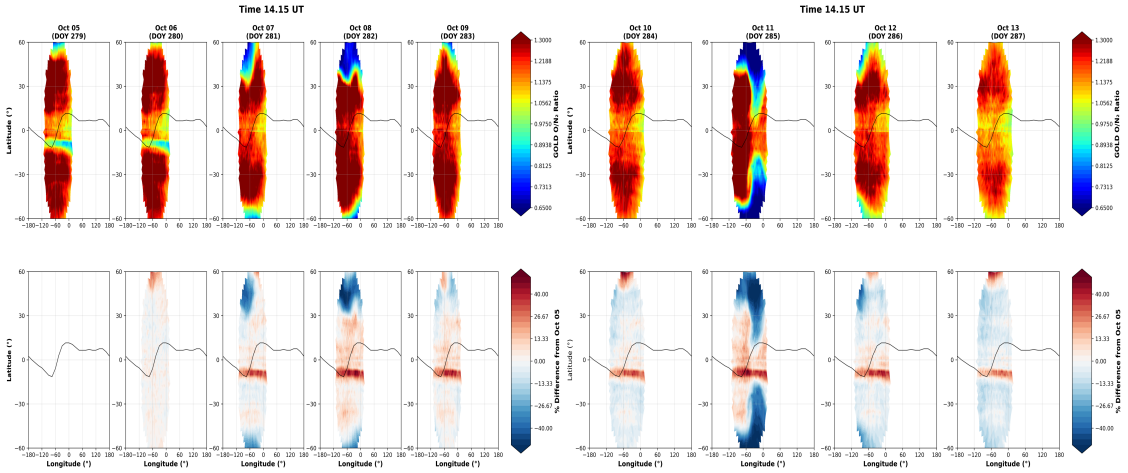

Figure 4. Thermospheric circulations during the October 2024 geomagnetic storm at 14.15 UT. The plot from NASA-GOLD illustrates the thermospheric circulation patterns observed from October 5 to October 13 (DOY 279 - 287).

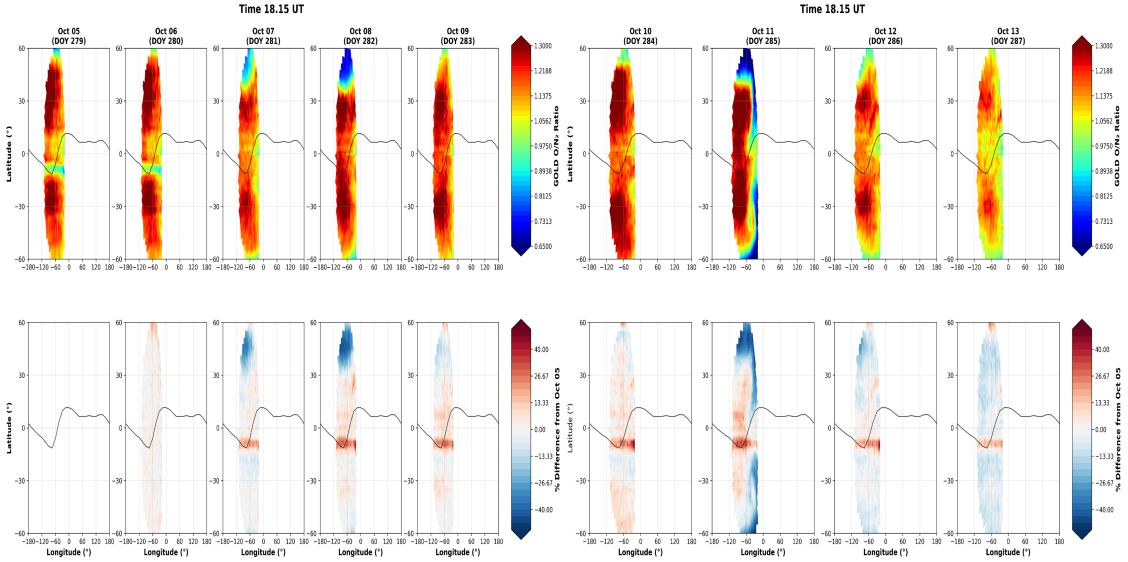

Figure 5. Thermospheric circulations during the October 2024 geomagnetic storm at 18.15 UT. The plot from NASA-GOLD illustrates the thermospheric circulation patterns observed from October 5 to October 13 (DOY 279 - 287).

The diurnal TEC peaks over HNUS at noon (at 12:00 UT), while that of RABT peaks in the post-noon period. The TEC observation over HNUS and RABT shows a similar pattern of TEC depletion of about $>$ 30 TECU and $>$ 50 TECU during the main phases of both the moderate and severe storms in October (see Figures 6 and 7), respectively. The TEC depletion is consistent with faster recombination of atmospheric atomic species and the N_2-dominated thermospheric advection [26], reducing the electron density in the ionosphere over the two stations.

 doi:10.20944/preprints202603.2324.v1

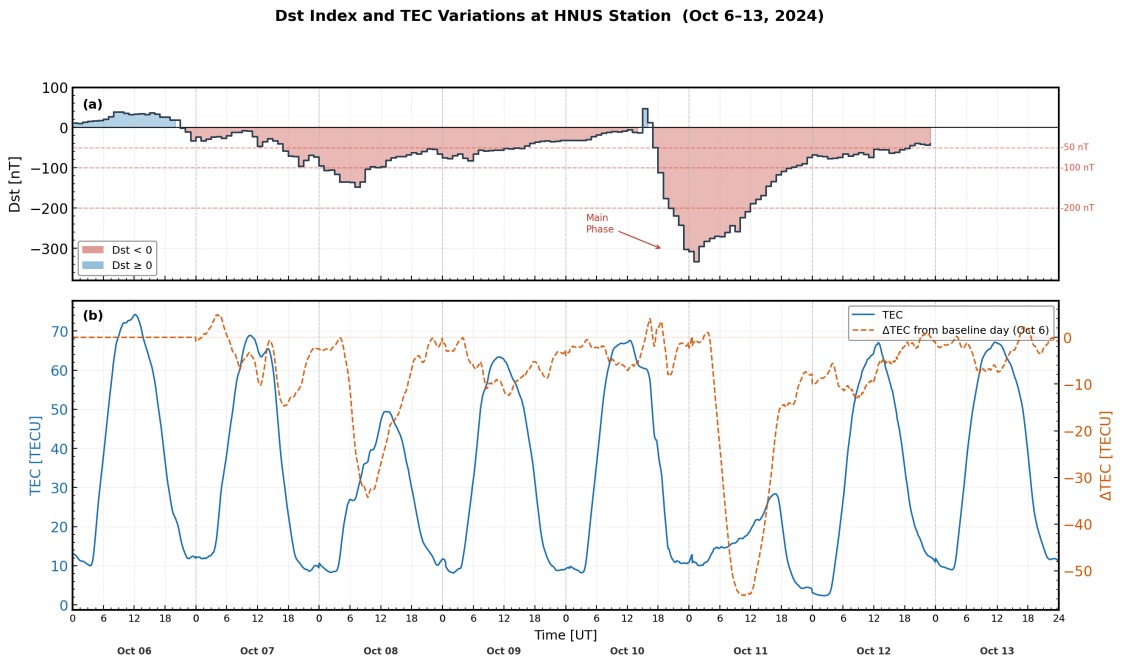

Figure 6. Two panel plots of the TEC and the *Dst*. The upper panel shows *Dst*, while the lower panel shows TEC over HNUS, plotted as the relative difference from the October 6 used as the baseline.

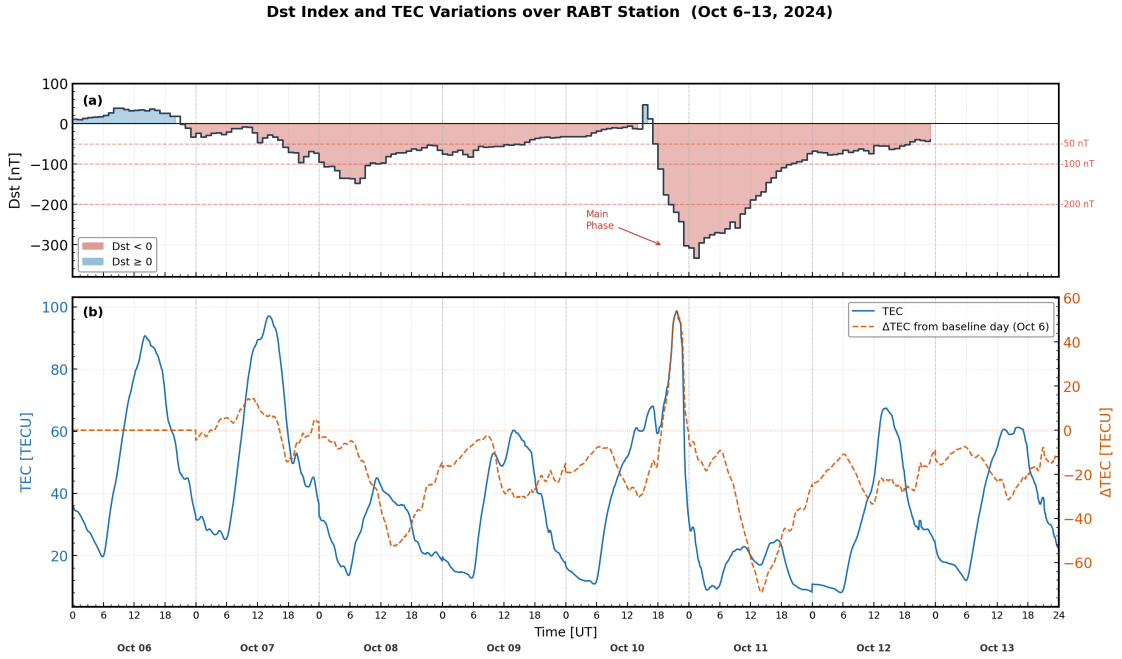

Figure 7. Two panel plots of the TEC and the *Dst*. The upper panel shows *Dst*, while the lower panel shows TEC over RABT, plotted relative to October 6, as the baseline.

This increase in N_2 at F-region altitudes (450 km) introduces a more rapid loss mechanism for ionospheric plasma. The dominant O^+ ions undergo a fast charge-exchange reaction with the upswelling N_2 molecules ($O^+ + N_2 \rightarrow NO^+ + N$), and the resulting molecular ions (NO^+) then recombine with electrons much more quickly than O^+ ions do, leading to a net depletion of TEC (Figure 8) in the F-region resulting in the negative ionospheric storm observed.

 doi:10.20944/preprints202603.2324.v1

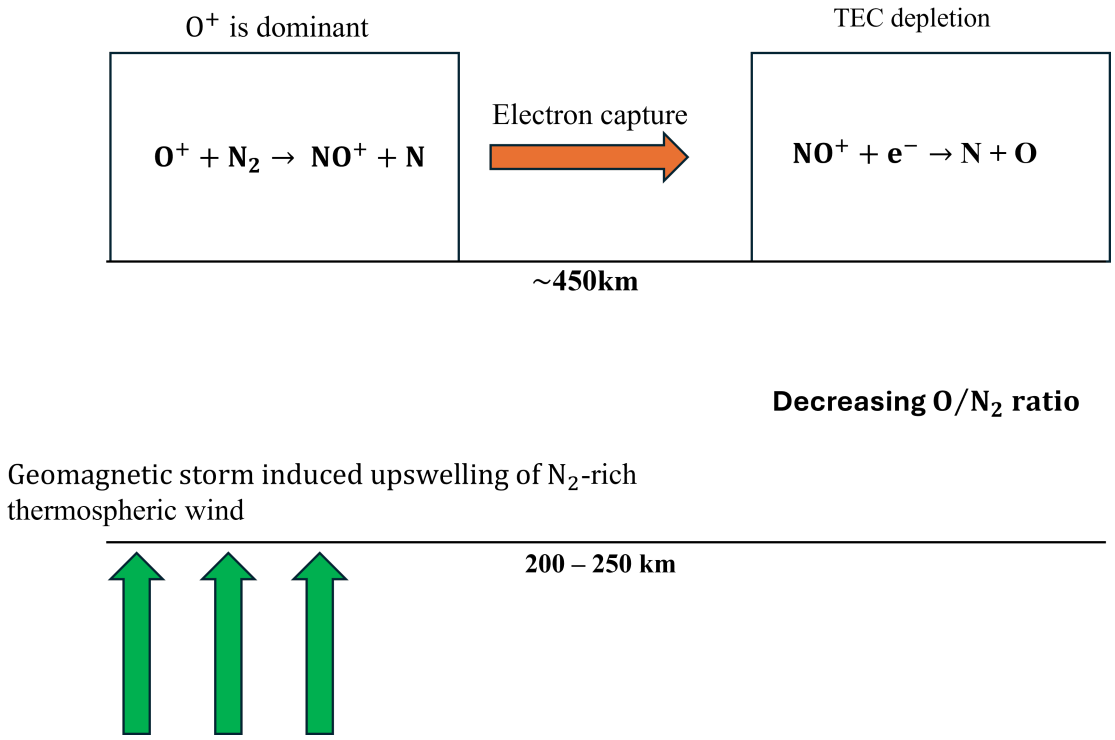

Figure 8. IT geomagnetic storm induced upswelling model. Induced thermospheric compositional changes and charge exchange reactions resulting in TEC depletion.

.induced thermospheric compositional changes and charge exchange

3.2. Storm-Time GNSS Positioning Accuracy

Figures 9 and 10 present the ECEF coordinate positioning errors (X, Y, Z components) at HNUS and RABT over Day of Year (DOY) 280–289, encompassing the storm commencement, the storm main phase, and the recovery phase of the October 2024 geomagnetic storm. At HNUS, a pronounced and coherent spike is observed simultaneously across all three ECEF components at DOY 285 during the main phase and early recovery phase, with the X-component reaching a maximum error of approximately 5.85 m, the Z-component 4.0 m, and the Y-component 2.45 m representing increases of roughly 270%, 150%, and 220%, respectively, relative to the October 6 (DOY 280) baseline values. This simultaneous degradation across all coordinate components at DOY 285 is consistent with a severe storm-time ionospheric negative phase over the Southern Hemisphere mid-latitudes, wherein TEC depletion to as low as 2.37 TECU, as observed in the TEC analysis, produces large unmodelled ionospheric residuals that project onto all three coordinate directions through the satellite geometry.

The SAMA-influenced irregular ionospheric structures over HNUS further prevent standard single-frequency ionospheric corrections from adequately absorbing the rapidly varying delay, amplifying positioning errors beyond what would be expected at a magnetically normal mid-latitude site. At RABT, in contrast, the positioning behaviour during DOY 285 is strikingly opposite; all three components reach their minimum errors for the entire observation window, with X reducing to 1.4 m, Y to 0.97 m, and Z to 3.1 m, compared to pre-main phase values of 6.7 m, 1.5 m, and 11.0 m, respectively, for DOY 280. This counter-intuitive improvement at the time of geomagnetic disturbance is consistent with a storm-time positive ionospheric phase over the Northern Hemisphere mid-latitudes driven by prompt penetration electric fields and the early-arriving equatorward thermospheric wind surge, which elevates plasma along field lines through the F-region wind dynamo, producing a smooth and spatially coherent TEC enhancement over the EIA crest that is readily corrected by the receiver. It is further noteworthy that RABT exhibits persistently large Z-component errors (8–11 m) throughout the period before storm's main phase, likely reflecting the station's proximity to the EIA crest, where elevated and structured background TEC inflates the vertical delay component even under geomag-

 doi:10.20944/preprints202603.2324.v1

netically quiet conditions, whereas the storm-time plasma uplift temporarily homogenises the spatial TEC structure, paradoxically improving the differential correction geometry. Figures 9 and 10 provide compelling observational evidence that storm-time GNSS positioning impact is not determined by the magnitude of geomagnetic disturbance alone, but critically by the sign and spatial structure of the ionospheric response at each station's magnetic and geographic location, degrading positioning where the ionosphere depletes and becomes irregular, while transiently improving it where the storm drives a coherent plasma enhancement.

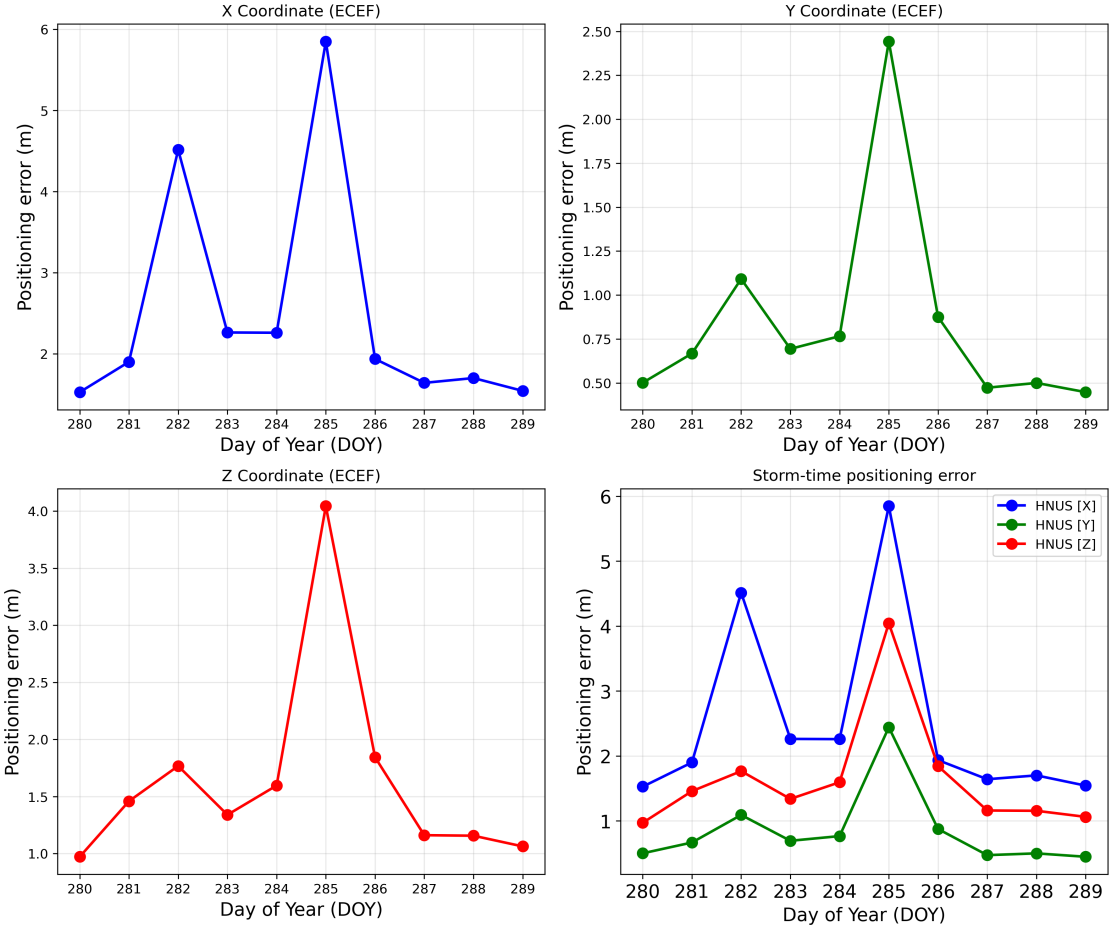

Figure 9. GNSS positioning accuracy over HNUS during the October storm. The absolute mean error in positioning on the ECEF coordinates over HNUS during the storm period, calculated using the same scheme as in [25,26].

 doi:10.20944/preprints202603.2324.v1

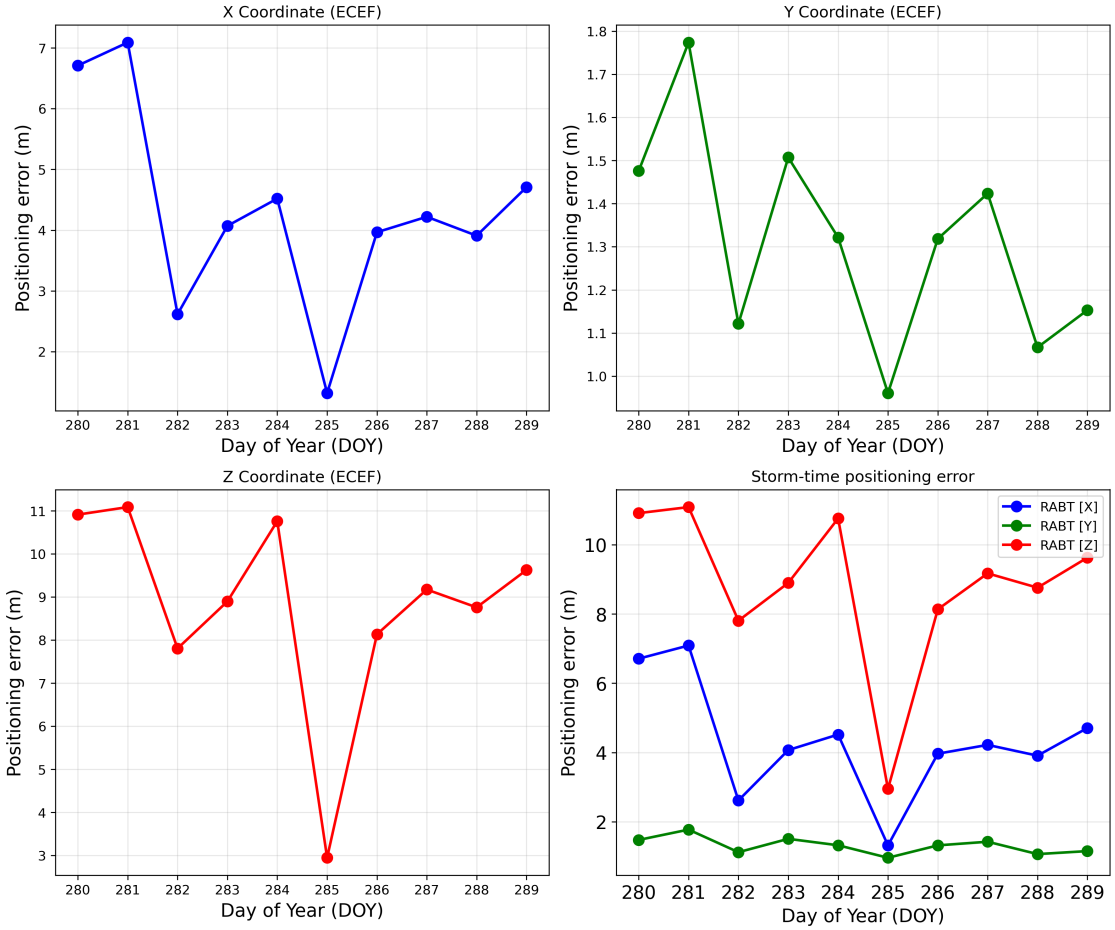

Figure 10. GNSS positioning accuracy during the October storm. The absolute mean error in positioning on the ECEF coordinates over RABT during the storm period.

4. Discussion

4.1. Dynamics and Energetics of the October 2024 Severe Storm

The severe geomagnetic storm of October 2024 was a complex two-step event initiated by the eruption of AR 13848 and multiple Coronal Mass Ejections (CMEs). The first step involved a moderate sudden storm commencement (SSC) on October 6 (DOY 280), reaching a minimum *Dst* of -148 nT on October 8 (DOY 282), while the subsequent severe SSC reached an extreme minimum Dst of -333 nT on October 11 (DOY 285). This extreme energy deposition from the solar wind exerted significant pressure on the magnetosphere, triggering intense Joule heating and particle precipitation at high latitudes e.g. [12,24]. Such heating leads to thermospheric expansion and circulation divergence, which fundamentally reshapes the composition of the upper atmosphere.

4.2. Physical Mechanisms of Ionosphere-Thermosphere (IT) Coupling

The primary physical mechanism driving the observed ionospheric response is the storm-time thermospheric upwelling. As heating occurs, air rich in molecular nitrogen (N_2) is transported from lower altitudes to the F-region (approximately 450 km). This upwelling significantly alters the neutral composition by lowering the O/N_2 ratio, which serves as the signature of a negative ionospheric storm e.g. [5,6,26]. In this enriched N_2 environment, the dominant O^+ ions undergo a rapid charge-exchange reaction. The resulting molecular ions (NO^+) recombine with electrons much faster than atomic oxygen ions do e.g. [16,33,34], leading to a net depletion of the Total Electron Content (TEC). Observations at the conjugate mid-latitude stations RABT and HNUS confirmed this consistent depletion, with TEC losses exceeding 30 TECU and 50 TECU during the moderate and severe phases, respectively.

 doi:10.20944/preprints202603.2324.v1

4.3. Hemispheric Asymmetry in Atmospheric Dynamics

This study highlights a critical hemispheric asymmetry in the propagation of thermospheric disturbances. NASA GOLD observations during the October 2024 storm main phase showed that N_2-dominated wind was advected equatorward in both hemispheres. However, a distinct difference was noted compared to the extreme storm of May 2024 [4,26]: in the October event, the equatorward thermospheric circulation in the Northern Hemisphere arrived before that of the Southern Hemisphere, the opposite is the case during the May 2024 events. This variability underscores the complexity of the geospace response and suggests that seasonal or Universal Time (UT) dependencies heavily influence how circulation patterns advect composition bulges toward lower latitudes.

4.4. Technological Implications for GNSS Positioning

During the October 2024 geomagnetic storm, the TEC observations at HNUS and RABT reveal a striking inter-hemispheric asymmetry in both ionospheric response and its consequence for GNSS positioning, one that cannot be fully explained by storm-time chemistry alone but requires consideration of storm-time thermospheric wind dynamics. At high latitudes, Joule heating and auroral particle precipitation deposit large amounts of energy into the thermosphere, launching equatorward neutral wind surges in both hemispheres. Critically however, the Northern Hemisphere wind surge arrives at mid-latitudes earlier than its Southern Hemisphere counterpart, a well-documented asymmetry attributable to the fact that during October, the Northern Hemisphere auroral oval is tilted toward the sun-lit dayside, where background thermospheric pressure gradients already favour equatorward flow, whereas the Southern Hemisphere surge must propagate through a relatively denser, more resistive nightside thermosphere e.g. [4,7]. This timing asymmetry has profoundly different ionospheric consequences at the two stations. Over RABT, the early-arriving northward-to-equatorward wind pushes ionospheric plasma upward along magnetic field lines through the F-region wind dynamo mechanism through the fountain effect enhancement, thereby elevating the F-layer to higher altitudes where recombination rates are lower, temporarily sustaining or even enhancing TEC and reinforcing the EIA crest e.g. [3].

This produces the elevated TEC observed at RABT during the storm onset, which, despite its higher absolute magnitude, remains tractable for dual-frequency GNSS receivers and spatially coherent enough for differential corrections to remain valid even during the TEC depletion that follows. Over HNUS, the delayed Southern Hemisphere equatorward wind surge arrives in an ionosphere already depleted by the negative storm-phase composition changes; the decrease in the O/N_2 ratio suppresses electron production that propagates from the auroral zone e.g. [6,28]. Rather than elevating plasma, the equatorward wind over the Southern Hemisphere mid-latitudes drives plasma downward along the steeper southern magnetic field lines into regions of higher recombination, accelerating the TEC depletion already underway and driving TEC as low as 2.37 TECU over the station. This downward plasma transport is particularly severe at HNUS owing to its location within the South Atlantic Magnetic Anomaly (SAMA) e.g. [27], where the anomalously shallow magnetic field inclination alters the effective projection of the neutral wind onto the field-aligned direction, amplifying the downward drift component relative to what would occur at a magnetically normal mid-latitude site. The consequence for GNSS is decisive: while RABT benefits from a wind-driven plasma uplift that produces high but smooth and correctable TEC, HNUS suffers a wind-accelerated plasma drainage that creates severe depletions, spatially incoherent structures, and large residual errors after ionospheric model correction e.g. [23], creating the observed GNSS positioning degradation.

5. Conclusions

This study analysed the upper atmospheric response over mid-latitude African stations to the severe geomagnetic storm of October 2024. We identified a consistent chain of cause and effect where storm-time thermospheric heating drove the upward transport of N_2-rich air, significantly increasing N_2 density at F-region altitudes (450 km) and lowering the O/N_2 ratio. This enrichment created an

 doi:10.20944/preprints202603.2324.v1

efficient pathway for the loss of ionospheric plasma through rapid charge-exchange reactions, leading to the significant TEC depletions characteristic of a negative ionospheric storm.

The study further reveals a critical inter-hemispheric timing asymmetry; the Northern Hemisphere wind surge arrived earlier than its Southern Hemisphere counterpart due to the October auroral oval tilt and background pressure gradients favouring equatorward flow in the north. The technological consequences of this asymmetry were decisive and contrasting. At RABT, the early wind surge drove a smooth plasma uplift that temporarily enhanced positioning geometry. Conversely, at HNUS, the delayed surge arrived in an already depleted ionosphere and, exacerbated by the South Atlantic Magnetic Anomaly (SAMA), drove plasma downward into regions of high recombination, resulting in severe positioning degradation. These outcomes highlight that under specific storm conditions, the geospace response can counterintuitively enhance positioning performance in one hemisphere while severely compromising it in another, reinforcing the complexity of the upper atmospheric response to geomagnetic storms.

Author Contributions: Conceptualization and methodology, J.O.; software, J.O.; validation, J.O., and D.M.; formal analysis, J.O.; investigation, J.O. and D.M.; resources, J.O. and D.M.; data curation, J.O. and D.M.; writing—original draft preparation, J.O.; writing—review and editing, J.O. and D.M.; visualization, J.O.; supervision, J.O.; project administration, J.O. All authors have read and agreed to the published version of the manuscript.

Funding: This research received no external funding.

Institutional Review Board Statement: Not applicable.

Informed Consent Statement: Not applicable.

Data Availability Statement: All datasets used in this study are publicly available and the links are provided in subsection 2.3 of this manuscript.

Acknowledgments: The data used in this study were made available through the following providers: The interplanetary and geomagnetic activity indices from the OmniWeb database hosted by NASA/GSFC Space Physics Data Facility, the IONOLAB, the NASA GOLD mission for GOLD data, The authors have reviewed and edited the output and take full responsibility for the content of this publication.

Conflicts of Interest: The authors declare no conflicts of interest.

References

1. Arikan F, Erol CB, Arikan O (2003) Regularized estimation of vertical total electron content from Global Positioning System data. J. Geophys. Res. 108:2002JA009605. doi:10.1029/2002JA009605
2. Arikan F, Nayir H, Sezen U, Arikan O (2008) Estimation of single station interfrequency receiver bias using GPS-TEC. Radio Science 43:2007RS003785. doi:10.1029/2007RS003785
3. Balan N, Liu L, Le H (2018) A brief review of equatorial ionization anomaly and ionospheric irregularities. Earth and Planetary Physics 2:1–19. doi:10.26464/epp2018025
4. Correira J, Evans JS, Lumpe JD, Eastes RW, Wang W, Aryal S, Krywonos A, McClintock WE (2024) Upper Atmospheric Vortices Following Strong Geomagnetic Storms. Authorea. doi:10.22541/essoar.173282311.17901375/v1
5. Fernandez-Gomez I, Kodikara T, Borries C, Forootan E, Goss A, Schmidt M, Codrescu MV (2022) Improving estimates of the ionosphere during geomagnetic storm conditions through assimilation of thermospheric mass density. Earth Planets Space 74:121. doi:10.1186/s40623-022-01678-3
6. Fuller-Rowell TJ, Codrescu MV, Moffett RJ, Quegan S (1994) Response of the thermosphere and ionosphere to geomagnetic storms. Journal of Geophysical Research: Space Physics 99:3893-3914. doi:10.1029/93JA02015
7. Fuller-Rowell TJ, Codrescu MV, Rishbeth H, Moffett RJ, Quegan S (1996) On the seasonal response of the thermosphere and ionosphere to geomagnetic storms. J. Geophys. Res. 101:2343–2353. doi:10.1029/95JA01614
8. Greer KR, Laskar F, Eastes RW, Lumpe J, Liu H-L, Pedatella N (2022) The Molecular Oxygen Density Structure of the Lower Thermosphere as Seen by GOLD and Models. Geophys Res Lett 49:e2022GL098800. doi:10.1029/2022GL098800
9. Guo J, Wang B, Whitman K, Plainaki C, Zhao L, Bain HM, Cohen C, Dalla S, Dumbovic M, Janvier M, Jun I, Luhmann J, Malandraki OE, Leila Mays M, Rankin JS, Wang L, Zheng Y (2024) Particle radiation

 doi:10.20944/preprints202603.2324.v1

environment in the heliosphere: Status, limitations, and recommendations. Advances in Space Research. doi:10.1016/j.asr.2024.03.070

10. Habarulema JB, Katamzi-Joseph ZT, Burešová D, Nndanganeni R, Matamba T, Tshisaphungo M, Buchert S, Kosch M, Lotz S, Cilliers P, Mahrous A (2020) Ionospheric Response at Conjugate Locations During the 7-8 September 2017 Geomagnetic Storm Over the Europe-African Longitude Sector. J Geophys Res Space Phys 125:e28307. doi:10.1029/2020JA028307
11. Jackman CH, DeLand MT, Labow GJ, Fleming EL, Weisenstein DK, Ko MKW, Sinnhuber M, Anderson J, Russell JM (2005) The influence of the several very large solar proton events in years 2000–2003 on the neutral middle atmosphere. Advances in Space Research 35:445-450. doi:10.1016/j.asr.2004.09.006
12. Jebaraj IC, Kouloumvakos A, Dresing N, Warmuth A, Wijsen N, Palmroos C, Gieseler J, Marmyleva A, Vainio R, Krupar V, Wiegelmann T, Magdalenic J, Schuller F, Battaglia AF, Fedeli A (2023) Multiple injections of energetic electrons associated with the flare and CME event on 9 October 2021. A&A 675:A27. doi:10.1051/0004-6361/202245716
13. Kalakoski N, Verronen PT, Seppala A, Szelag ME, Kero A, Marsh DR (2020) Statistical response of middle atmosphere composition to solar proton events in WACCM-D simulations: the importance of lower ionospheric chemistry. Atmos Chem Phys 20:8923-8938. doi:10.5194/acp-20-8923-2020
14. Kim J, Kwak Y-S, Lee C, Lee J, Kam H, Yang T-Y, Jee G, Kim YH (2023) Observational evidence of thermospheric wind and composition changes and the resulting ionospheric disturbances in the European sector during extreme geomagnetic storms. J. Space Weather Space Clim. 13:24. doi:10.1051/swsc/2023025
15. Kolarski A, Veselinović N, Srećković VA, Mijić Z, Savić M, Dragić A (2023) Impacts of Extreme Space Weather Events on September 6th, 2017 on Ionosphere and Primary Cosmic Rays. Remote Sens 15:1403. doi:10.3390/rs15051403
16. Krall J, Huba JD (2021) The Effect of the Thermosphere on Ionosphere Outflows. Front. Astron. Space Sci. 8:712616. doi:10.3389/fspas.2021.712616
17. Li W, Liu T, Zuo P, Zou Z, Ruan M, Wei J (2024) Low-latitude ionospheric responses and positioning performance of ground GNSS associated with the geomagnetic storm on March 13–14, 2022. Front Astron Space Sci 11:1431611. doi:10.3389/fspas.2024.1431611
18. Mansilla GA (2011). Some effects in the upper atmosphere during geomagnetic storms. Advances in Space Research 47:930-937. doi:10.1016/j.asr.2010.11.017
19. Matamba TM, Danskin DW, Nndanganeni RR, Tshisaphungo M (2023) Space weather impacts on the ionosphere over the southern African mid-latitude region. Earth Planets Space 75:142. doi:10.1186/s40623-023-01894-5
20. Mironova I, Sinnhuber M, Bazilevskaya G, Clilverd M, Funke B, Makhmutov V, Rozanov E, Santee ML, Sukhodolov T, Ulich T (2022) Exceptional middle latitude electron precipitation detected by balloon observations: implications for atmospheric composition. Atmospheric Chemistry and Physics 22:6703-6716. doi:10.5194/acp-22-6703-2022
21. Nanjo S, Shiokawa K (2024) Spatial structures of blue low-latitude aurora observed from Japan during the extreme geomagnetic storm of May 2024. Earth, Planets and Space 76:156. doi:10.1186/s40623-024-02090-9
22. Nava B, Rodríguez-Zuluaga J, Alazo-Cuartas K, Kashcheyev A, Migoya-Orué Y, Radicella SM, Amory-Mazaudier C, Fleury R (2016) Middle- and low-latitude ionosphere response to 2015 St. Patrick's Day geomagnetic storm. J Geophys Res Space Phys 121:3421-3438. doi:10.1002/2015JA022299
23. Nava B, Coïsson P, Radicella SM (2008) A new version of the NeQuick ionosphere electron density model. Journal of Atmospheric and Solar-Terrestrial Physics 70:1856–1862. doi:10.1016/j.jastp.2008.01.015
24. Nilam B, Tulasi Ram S, Oliveira DM, Remya B, Shiokawa K, Rai D, Sibeck D, Dimri AP (2025) Strong Westward Current Pulse at Auroral Latitudes Extending to Dawn-Side Low-Latitudes Due To Enhanced Density Within Kelvin-Helmholtz Wave Vortex in Solar Wind. Geophysical Research Letters 52:e2025GL117032. doi:10.1029/2025GL117032
25. Omojola J, Adewumi T (2019) Effects of St Patrick's Day Intervals Geomagnetic Storms on the Accuracy of GNSS Positioning and Total Electron Content over Nigeria. JESP Online First. doi:10.22059/jesphys.2019.259772.1007014
26. Omojola J, Greer K, Moeketsi D (2025) Geospace response to May 2024 X-class flare and coronal mass ejection. Adv Space Res. doi:10.1016/j.asr.2025.04.036
27. Pavón-Carrasco FJ, De Santis A (2016) The South Atlantic Anomaly: The Key for a Possible Geomagnetic Reversal. Front. Earth Sci. 4. doi:10.3389/feart.2016.00040

 doi:10.20944/preprints202603.2324.v1

28. Prölss GW (2011) Density Perturbations in the Upper Atmosphere Caused by the Dissipation of Solar Wind Energy. Surv Geophys 32:101-195. doi:10.1007/s10712-010-9104-0
29. Qian L, Solomon SC (2012) Thermospheric Density: An Overview of Temporal and Spatial Variations. Space Sci Rev 168:147-173. doi:10.1007/s11214-011-9810-z
30. Qian L, Gan Q, Wang W, Cai X, Eastes R, Yue J (2022) Seasonal Variation of Thermospheric Composition Observed by NASA GOLD. JGR Space Physics 127:e2022JA030496. doi:10.1029/2022JA030496
31. Ratovsky KG, Klimenko MV, Yasyukevich YV, Klimenko VV, Vesnin AM (2020) Statistical Analysis and Interpretation of High-, Mid- and Low-Latitude Responses in Regional Electron Content to Geomagnetic Storms. Atmosphere 11:1308. doi:10.3390/atmos11121308
32. Sezen U, Arikan F, Arikan O, Ugurlu O, Sadeghimorad A (2013) Online, automatic, near-real time estimation of GPS-TEC: IONOLAB-TEC. Space Weather 11:297–305. doi:10.1002/swe.20054
33. Shahzad R, Shah M, Tariq MA, Calabia A, Melgarejo-Morales A, Jamjareegulgarn P, Liu L (2023) Ionospheric–Thermospheric Responses to Geomagnetic Storms from Multi-Instrument Space Weather Data. Remote Sensing 15:2687. doi:10.3390/rs15102687
34. Sojka JJ, Schunk RW (1984) A theoretical F region study of ion compositional and temperature variations in response to magnetospheric storm inputs. J. Geophys. Res. 89:2348–2358. doi:10.1029/JA089iA04p02348
35. Tulasi Ram S, Veenadhari B, Dimri AP, Bulusu J, Bagiya M, Gurubaran S, Parihar N, Remya B, Seemala G, Singh R, Sripathi S, Singh SV, Vichare G (2024) Super-Intense Geomagnetic Storm on 10–11 May 2024: Possible Mechanisms and Impacts. Space Weather 22:e2024SW004126. doi:10.1029/2024SW004126
36. Velinov PIY, Asenovski S, Kudela K, Lastovicka J, Mateev L, Mishev A, Tonev P (2013) Impact of cosmic rays and solar energetic particles on the Earth's ionosphere and atmosphere. J Space Weather Space Clim 3:A14. doi:10.1051/swsc/2013036